GEOPHYSICS, VOL. 79, NO. 3 (MAY-JUNE 2014); P. T157–T168, 16 FIGS.
10.1190/GEO2013-0290.1

Lowrank seismic-wave extrapolation on a staggered grid

Gang Fang[1], Sergey Fomel[2], Qizhen Du[1], and Jingwei Hu[3]

ABSTRACT

We evaluated a new spectral method and a new finite-difference (FD) method for seismic-wave extrapolation in time. Using staggered temporal and spatial grids, we derived a wave-extrapolation operator using a lowrank decomposition for a first-order system of wave equations and designed the corresponding FD scheme. The proposed methods extend previously proposed lowrank and lowrank FD wave extrapolation methods from the cases of constant density to those of variable density. Dispersion analysis demonstrated that the proposed methods have high accuracy for a wide wavenumber range and significantly reduce the numerical dispersion. The method of manufactured solutions coupled with mesh refinement was used to verify each method and to compare numerical errors. Tests on 2D synthetic examples demonstrated that the proposed method is highly accurate and stable. The proposed methods can be used for seismic modeling or reverse-time migration.

INTRODUCTION

Wave extrapolation in time is an essential part of seismic imaging, modeling, and full-waveform inversion. Finite-difference (FD) methods (Etgen, 1986; Wu et al., 1996) and spectral methods (Tal-Ezer et al., 1987; Reshef et al., 1988) are the two most popular and straightforward ways of implementing wave extrapolation in time. The FD methods are highly efficient and easy to implement. However, the traditional FD methods are only conditionally stable and suffer from numerical dispersion (Finkelstein and Kastner, 2007). Thanks to advances in supercomputer technology, spectral methods have become feasible for large-scale problems. Compared with FD methods, spectral methods have superior accuracy and are able to suppress dispersion artifacts (Etgen and Brandsberg-Dahl, 2009).

Several spectral methods have been developed for seismic-wave extrapolation in variable-velocity media (Fowler et al., 2010; Du et al., 2014). Zhang et al. (2007) and Zhang and Zhang (2009) propose a one-step extrapolation algorithm, which is derived from an optimized separable approximation (OSA). This algorithm formulates the two-way wave equation as a first-order partial differential equation in time without suffering from numerical instability or dispersion problems. Soubaras and Zhang (2008) propose a two-step extrapolation method that is based on a high-order differential operator, which allows for large time steps in extrapolation. However, the decomposition algorithm in OSA can be expensive, particularly in anisotropic media. Fomel et al. (2013b) present an approach to approximating the mixed-domain operator using a lowrank decomposition, which reduces computational cost by optimally selecting reference velocities and weights. Song and Fomel (2011) develop a related method, Fourier finite-differences (FFDs), by cascading a Fourier transform operator and an FD operator to form a chain operator.

In practice, first-order wave equations are often involved in handling wave extrapolation in media with velocity and density variations. Mast et al. (2001) provide a derivation of the k-space method for solving the ultrasonic wave equation. Tabei et al. (2002) extend this method to solving coupled first-order differential equations for wave propagation, efficiently accounting for velocity and density variations. In the k-space method, dispersion errors from a second-order time integration operator are compensated by a modified spectral operator in the wavenumber domain. This correction is exact for a medium with constant velocity in particular. Song et al. (2012) modify the k-space method with a mixed-domain operator and apply FFD to handle these operators. This method has high accuracy for variable velocity and density.

In the FD methods, the FD coefficients are conventionally determined through a Taylor-series expansion around the zero

Manuscript received by the Editor 31 July 2013; revised manuscript received 4 January 2014; published online 27 May 2014.
[1]China University of Petroleum (East China), School of Geosciences, Qingdao, Shandong, China. E-mail: fangg.geo@gmail.com; multicomponent@163.com.
[2]The University of Texas at Austin, Bureau of Economic Geology, John A. and Katherine G. Jackson School of Geosciences, Austin, Texas, USA. E-mail: sergey.fomel@beg.utexas.edu.
[3]The University of Texas at Austin, Institute for Computational Engineering and Sciences (ICES), Austin, Texas, USA. E-mail: hu@ices.utexas.edu.

wavenumber (Dablain, 1986; Kindelan et al., 1990). Traditional FD methods are therefore particularly accurate for long-wavelength components. Several approaches have been proposed to improve the performance of the FD method in practice. Implicit FD operators (Liu and Sen, 2009; Chu and Stoffa, 2011) can be used to achieve high-numerical accuracy. Another way to control numerical errors is to use optimized FD operators (Takeuchi and Geller, 2000; Chu et al., 2009; Liu, 2013). Song et al. (2013) derive optimized coefficients of the FD operator from a lowrank approximation (Fomel et al., 2013b) of the space-wavenumber extrapolation matrix. To improve the accuracy and stability, the FD methods have been developed on a staggered grid (Madariaga, 1976; Virieux, 1984, 1986; Levander, 1988). Moczo et al. (2002) investigate the stability and grid dispersion in the 3D fourth-order staggered-grid FD scheme. In the past few years, viscous wave modeling using staggered-grid FD methods (Robertsson et al., 1994; Bohlen, 2002; Operto et al., 2007) has also been studied and reported.

In this paper, we use a modified staggered-grid k-space method (Tabei et al., 2002; Song et al., 2012) to handle the derivative operator in the mixed domain for variable velocity and density. We introduce lowrank decomposition (Fomel et al., 2013b) to approximate the modified k-space extrapolation operator and reduce the computational cost. Inspired by lowrank FDs (Song et al., 2013), we derive optimized FD coefficients for coupled first-order wave-propagation equations using staggered spatial and temporal grids (Virieux, 1984, 1986; Levander, 1988). We apply dispersion analysis and use the method of manufactured solutions (MMS) to evaluate the accuracy of the proposed methods. Numerical tests demonstrate that the proposed staggered-grid lowrank (SGL) and staggered-grid lowrank finite-differences (SGLFD) methods are highly accurate and applicable for variable velocity and density modeling and reverse time migration (RTM) in complicated models. Our implementation of the new methods and the numerical examples are based on Madagascar software (Fomel et al., 2013a) and can be reproduced using the latest version of Madagascar.

THEORY

Second- and first-order mixed-domain methods

We consider first-order acoustic wave equations for a medium of variable velocity and density. For a lossless 2D medium,

$$\rho(\mathbf{x})\frac{\partial \mathbf{u}(\mathbf{x},t)}{\partial t} = -\nabla p(\mathbf{x},t),$$
$$\frac{1}{\rho(\mathbf{x})v^2(\mathbf{x})}\frac{\partial p(\mathbf{x},t)}{\partial t} = -\nabla\cdot\mathbf{u}(\mathbf{x},t), \quad (1)$$

where $\mathbf{u}(\mathbf{x},t)$ is the acoustic particle velocity with components $u_x(\mathbf{x},t)$ and $u_z(\mathbf{x},t)$, $p(\mathbf{x},t)$ is the acoustic pressure, $\rho(\mathbf{x})$ is the density of the medium, $v(\mathbf{x})$ is the seismic wave velocity of the medium, and $\mathbf{x}=(x,z)$ denotes the space location in the vector coordinate.

The second-order wave equation corresponding to equation 1 is

$$\nabla\cdot\frac{1}{\rho(\mathbf{x})}\nabla p(\mathbf{x},t) - \frac{1}{\rho(\mathbf{x})v^2(\mathbf{x})}\frac{\partial^2 p(\mathbf{x},t)}{\partial t^2} = 0. \quad (2)$$

In the case of homogeneous velocity and density, equation 2 can be written in the spatial-frequency domain as

$$\frac{\partial^2 \hat{p}(\mathbf{k},t)}{\partial t^2} = -v_0^2\mathbf{k}^2\hat{p}(\mathbf{k},t), \quad (3)$$

where $\hat{p}(\mathbf{k},t)$ is the 2D spatial Fourier transform of $p(\mathbf{x},t)$. Equation 3 has an analytical solution:

$$\hat{p}(\mathbf{k},t+\Delta t) = e^{\pm iv_0|\mathbf{k}|\Delta t}\hat{p}(\mathbf{k},t). \quad (4)$$

Applying the second-order time-marching scheme leads to the k-space scheme (Tabei et al., 2002):

$$\frac{\hat{p}(\mathbf{k},t+\Delta t) - 2\hat{p}(\mathbf{k},t) + \hat{p}(\mathbf{k},t-\Delta t)}{\Delta t^2} = -(v_0|\mathbf{k}|)^2\mathrm{sinc}^2(v_0|\mathbf{k}|\Delta t/2)\hat{p}(\mathbf{k},t), \quad (5)$$

where $\mathrm{sinc}(x)=\sin(x)/x$. In general, velocity and density vary in space. When the gradient of velocity and the time step are small, replacing v_0 with $v(\mathbf{x})$ in equation 5 provides a new approximation. Applying inverse Fourier transform to this approximation leads to the scheme,

$$\frac{p(\mathbf{x},t+\Delta t) - 2p(\mathbf{x},t) + p(\mathbf{x},t-\Delta t)}{\Delta t^2} = -v^2(\mathbf{x})\mathbf{F}^{-1}[|\mathbf{k}|^2\mathrm{sinc}^2(v(\mathbf{x})|\mathbf{k}|\Delta t/2)\mathbf{F}[p(\mathbf{x},t)]], \quad (6)$$

where $\mathbf{F}$ denotes a spatial Fourier transform. The operator on the right-hand side of equation 6 depends on $\mathbf{x}$ and $\mathbf{k}$. Following Tabei et al. (2002), we call it the second-order kx-space operator:

$$[\nabla^{v(\mathbf{x})\Delta t}]^2 p(\mathbf{x},t) \equiv -\mathbf{F}^{-1}[|\mathbf{k}|^2\mathrm{sinc}^2(v(\mathbf{x})|\mathbf{k}|\Delta t/2)\mathbf{F}[p(\mathbf{x},t)]], \quad (7)$$

where the operator $[\nabla^{v(\mathbf{x})\Delta t}]^2$ is analogous to the standard gradient operator, but it is a function of parameter $v(\mathbf{x})\Delta t$. Similar to the definition of the standard gradient operator, we can define

$$[\nabla^{v(\mathbf{x})\Delta t}]^2 p(\mathbf{x},t) \equiv \left(\frac{\partial}{\partial^+ x}\frac{\partial}{\partial^- x} + \frac{\partial}{\partial^+ z}\frac{\partial}{\partial^- z}\right)p(\mathbf{x},t). \quad (8)$$

Tabei et al. (2002) suggest a factorization that can factor their second-order k-space operator into parts associated with each spatial direction. This factorization can also be applied to the kx-space operator by replacing constant velocity with variable velocity. The factored operators are called first-order kx-space operators:

$$\frac{\partial p(\mathbf{x},t)}{\partial^+ x} \equiv \mathbf{F}^{-1}[ik_x e^{ik_x\Delta x/2}\mathrm{sinc}(v(\mathbf{x})|\mathbf{k}|\Delta t/2)\mathbf{F}[p(\mathbf{x},t)]],$$
$$\frac{\partial p(\mathbf{x},t)}{\partial^- x} \equiv \mathbf{F}^{-1}[ik_x e^{-ik_x\Delta x/2}\,\mathrm{sinc}(v(\mathbf{x})|\mathbf{k}|\Delta t/2)\mathbf{F}[p(\mathbf{x},t)]],$$
$$\frac{\partial p(\mathbf{x},t)}{\partial^+ z} \equiv \mathbf{F}^{-1}[ik_z e^{ik_z\Delta z/2}\,\mathrm{sinc}(v(\mathbf{x})|\mathbf{k}|\Delta t/2)\mathbf{F}[p(\mathbf{x},t)]],$$
$$\frac{\partial p(\mathbf{x},t)}{\partial^- z} \equiv \mathbf{F}^{-1}[ik_z e^{-ik_z\Delta z/2}\,\mathrm{sinc}(v(\mathbf{x})|\mathbf{k}|\Delta t/2)\mathbf{F}[p(\mathbf{x},t)]]. \quad (9)$$

The spatial frequency components k_x and k_z are defined so that $k^2 = k_x^2 + k_z^2$. Application of the exponential coefficient in equation 9 requires the corresponding wavefield to be evaluated on grid

points staggered by a distance of $\Delta x/2$ along the positive or negative x-direction and $\Delta z/2$ along the positive or negative z-direction. The spatial staggering in equation 9 is implicitly incorporated into the spatial derivative by the shift property of the Fourier transform. Using operators in equation 9 within equation 1 enables a new construction of spectral method. The first-order coupled equations for acoustic-wave extrapolation in variable velocity and density media with staggered spatial and temporal grids are, therefore,

$$\begin{aligned}
\frac{u_x(\mathbf{x}_1,t^+)-u_x(\mathbf{x}_1,t^-)}{\Delta t} &= -\frac{1}{\rho(\mathbf{x}_1)}\frac{\partial p(\mathbf{x},t)}{\partial^+ x},\\
\frac{u_z(\mathbf{x}_2,t^+)-u_z(\mathbf{x}_2,t^-)}{\Delta t} &= -\frac{1}{\rho(\mathbf{x}_2)}\frac{\partial p(\mathbf{x},t)}{\partial^+ z},\\
\frac{p(\mathbf{x},t+\Delta t)-p(\mathbf{x},t)}{\Delta t} &= -\rho(\mathbf{x})v^2(\mathbf{x})\left(\frac{\partial u_x(\mathbf{x}_1,t^+)}{\partial^- x}\right.\\
&\quad\left.+\frac{\partial u_z(\mathbf{x}_2,t^+)}{\partial^- z}\right),
\end{aligned} \tag{10}$$

where $\mathbf{x}_1 \equiv (x+\Delta x/2, z)$, $\mathbf{x}_2 \equiv (x, z+\Delta z/2)$, $t^+ \equiv t+\Delta t/2$, and $t^- \equiv t-\Delta t/2$.

The partial derivative operators in equation 10 are defined by equation 9. Note that the ordering of $\partial/\partial^+ x$ and $\partial/\partial^- x$ is arbitrary depending on the configuration of the staggered grid. However, these operators should be used in pairs, such that the spatial shifting cancels out over any temporal interval length Δt. The spatial and temporal staggered grids used in equation 10 are analogous to the staggered scheme employed in previous FD methods (Madariaga, 1976; Virieux, 1984, 1986), which are known to increase accuracy and stability by halving spatial and time intervals without increasing the number of computational points. Equation 9 can be solved with a localized Fourier transform (Wards et al., 2008). However, this kind of solution has a high computational cost. Song et al. (2012) propose to apply FFD method to calculate the first-order kx-space operators in equation 9, which can handle the variable velocity and density accurately and efficiently. Another possible way to speed up the computation is to represent the extrapolation operator with a lowrank matrix.

Lowrank approximation for first-order extrapolation operators

In this section, we apply lowrank decomposition to approximate the extrapolation operator in equation 9. As indicated by Fomel et al. (2010, 2013b), the mixed-domain matrix in equation 9, taking $\frac{\partial p(\mathbf{x},t)}{\partial^+ x}$ as an example,

$$W_x(\mathbf{x},\mathbf{k}) = k_x \mathrm{sinc}(v(\mathbf{x})|\mathbf{k}|\Delta t/2), \tag{11}$$

can be efficiently decomposed into a separated representation as follows:

$$W_x(\mathbf{x},\mathbf{k}) \approx \sum_{m=1}^{M}\sum_{n=1}^{N} W_x(\mathbf{x},\mathbf{k}_m)a_{mn}W_x(\mathbf{x}_n,\mathbf{k}), \tag{12}$$

where $W_x(\mathbf{x},\mathbf{k}_m)$ is a submatrix of $W_x(\mathbf{x},\mathbf{k})$, which consists of selected columns associated with $\mathbf{k}_m$; $W_x(\mathbf{x}_n,\mathbf{k})$ is another submatrix that contains selected rows associated with $\mathbf{x}_n$; and a_{nm} stands for the middle matrix coefficients. The numerical construction of the separated representation in equation 12 follows the method of Engquist and Ying (2009).

Using representation 12, we can calculate $\frac{\partial p(\mathbf{x},t)}{\partial^+ x}$ using a small number of fast Fourier transforms (FFTs) because

$$\begin{aligned}
&\frac{\partial p(\mathbf{x},t)}{\partial^+ x}\\
&\approx \sum_{m=1}^{M}\sum_{n=1}^{N} W_x(\mathbf{x},\mathbf{k}_m)a_{mn}\mathbf{F}^{-1}[ie^{ik_x\Delta x/2}W_x(\mathbf{x}_n,\mathbf{k})\mathbf{F}[p(\mathbf{x},t)]].
\end{aligned} \tag{13}$$

The same lowrank decomposition approach can be applied to the remaining three partial derivative operators in equation 9. Evaluation of equation 13 only needs N inverse FFTs, whose computational cost is $O(NN_x \log N_x)$. However, a straightforward application of equation 9 needs the computational cost of $O(N_x^2)$, where N_x is the total size of the space grid. The value of N is related to the rank of the decomposed mixed-domain matrix 12, which is usually significantly smaller than N_x. Note that the number of FFTs N also depends on the given error level of lowrank decomposition with a predetermined Δt. Thus, a complex model or increasing the time interval size Δt may increase the rank of the approximation matrix and correspondingly N. In the numerical examples in this paper, the values of rank are usually between 2 and 4. Lowrank decomposition saves cost in calculating equations 9 and 10. We propose to apply it for seismic-wave extrapolation in variable velocity and density media on a staggered grid. We call this the SGL method.

Lowrank FD for first-order extrapolation operators

Approximation 12 can also be used to design accurate FD schemes. Here, we extend the lowrank FD method (Song et al., 2013) to first-order kx-space operators. Note that $W_x(\mathbf{x}_n,\mathbf{k})$ in equation 13 is a matrix related only to wavenumber $\mathbf{k}$. It can be further decomposed as follows:

$$W_x(\mathbf{x}_n,\mathbf{k}) \approx \sum_{l=1}^{L} C(\mathbf{x}_n,\xi_l)B(\xi_l,\mathbf{k}), \tag{14}$$

where B is an $L \times N_x$ matrix. Specifically, we can define $B(\xi_l,\mathbf{k})$ to take the form of $\sin(\sum_{j=1}^{3}\xi_l^j k_j \Delta_j)$, in which ξ_l^j is the jth component of a 3D vector, $\xi_l = (\xi_l^1, \xi_l^2, \xi_l^3)$; k_j is the jth component of wavenumber $\mathbf{k}$; Δ_j is the space grid size in the jth direction; $j = 1, 2, 3$ corresponds to x, y, z direction in space; and C is the matrix product of W_x and the pseudoinverse of B. If we define

$$G(\mathbf{x},l) = \sum_{m=1}^{M}\sum_{n=1}^{N} W_x(\mathbf{x},\mathbf{k}_m)a_{mn}C(\mathbf{x}_n,\xi_l), \tag{15}$$

then equation 13 can be described as

$$\frac{\partial p(\mathbf{x},t)}{\partial^+ x}$$
$$\approx \sum_{l=1}^{L} G(\mathbf{x},l)\mathbf{F}^{-1}[ie^{ik_x\Delta x/2}B(\mathbf{x}_n,\boldsymbol{\xi}_l)\mathbf{F}[p(\mathbf{x},t)]]$$
$$\approx \sum_{l=1}^{L} G(\mathbf{x},l)\mathbf{F}^{-1}\left[ie^{ik_x\Delta x/2}\sin\left(\sum_{j=1}^{3}\xi_l^j k_j\Delta_j\right)\mathbf{F}[p(\mathbf{x},t)]\right]$$
$$\approx \frac{1}{2}\sum_{l=1}^{L} G(\mathbf{x},l)\mathbf{F}^{-1}\left[e^{ik_x\Delta x/2}\left(e^{i\sum_{j=1}^{3}\xi_l^j k_j\Delta_j}\right.\right.$$
$$\left.\left.-e^{-i\sum_{j=1}^{3}\xi_l^j k_j\Delta_j}\right)\mathbf{F}[p(\mathbf{x},t)]\right]. \quad (16)$$

For a staggered grid, in which pressure is defined on main grid points and particle velocity on half-grid points, we can choose $\boldsymbol{\xi}_l$ as $\xi_l^1 = (2l^1-1)/2, \xi_l^2 = l^2, \xi_l^3 = l^3$ to calculate the partial derivative in the x-direction, where $l^1, l^2, l^3 = 1,2,\ldots,L$ and L is the length of the stencil. According to the shift property of FFTs, we can finally obtain the following expression in the space domain:

$$\frac{\partial p(\mathbf{x},t)}{\partial^+ x} \approx \frac{1}{2}\sum_{l=1}^{L} G(\mathbf{x},l)[P(\mathbf{x}_R,t) - P(\mathbf{x}_L,t)], \quad (17)$$

where $\mathbf{x}_R = (x_1 + l^1\Delta_1, x_2 + l^2\Delta_2, x_3 + l^3\Delta_3)$ and $\mathbf{x}_L = (x_1 - (l^1-1)\Delta_1, x_2 - l^2\Delta_2, x_3 - l^3\Delta_3)$.

Equation 17 corresponds to the procedure of FD scheme for calculating the kx-space operator. The vector $\boldsymbol{\xi}_l = (\xi_l^1, \xi_l^2, \xi_l^3)$ provides stencil information, and $G(\mathbf{x},l)$ stores the corresponding coefficients. A similar derivation can be applied to the remaining partial derivative operators in equation 9. We call this the SGLFD method.

Whereas the SGL method (equation 13) is proposed by applying lowrank approximation to the kx-space method on a staggered grid (equation 9), SGLFD (equation 17) is a further approximation of SGL. Theoretically, the SGLFD method, using a longer stencil, reaches higher accuracy. It is hard to derive the stability condition for SGL. However, applying Von Neumann stability analysis, we can easily obtain a sufficient condition of stability for SGLFD as

$$\left|\Delta t v_{\max}\sum_{l=1}^{L} G(x,l)\sin\left(\sum_{j=1}^{3}\xi_l^j k_j\Delta_j\right)\right| \le 1, \quad (18)$$

where $v_{\max}$ is the maximum value of velocity. Once we obtain the FD coefficient $G(\mathbf{x},l)$ for a certain velocity $v(\mathbf{x})$ and the predefined parameters Δ_j and Δt, we can use condition 18 to estimate the stability of the SGLFD scheme in equation 17.

Next, we use the plane-wave theory to evaluate numerical dispersion for SGLFD method. Inserting the plane-wave solution,

$$p(\mathbf{x},t) = p_0 e^{i\mathbf{k}\cdot\mathbf{x}-\omega t},$$
$$\mathbf{u}(\mathbf{x},t) = \mathbf{u}_0 e^{i\mathbf{k}\cdot\mathbf{x}-\omega t}, \quad (19)$$

into equation 17 and also adopting the dispersion relation $\omega = |\mathbf{k}|v$, the relative error of phase velocity is defined as

$$\varepsilon = \frac{v_{\mathrm{LFD}}}{v} - 1$$
$$= \frac{1}{\omega\Delta t}\arcsin\left(\sum_{l=1}^{L} G(\mathbf{x},l)\sum_{j=1}^{3}\sin(\xi_l^j k_j\Delta_j)\right) - 1. \quad (20)$$

The relative error ε describes the numerical dispersion of the SGLFD method. If ε equals 0, there is no dispersion. If ε is far from 0, a large dispersion will occur. Here, we define the order of SGLFD as that of conventional FD that has the same stencil length (L). Next, we compare the conventional staggered-grid finite-difference (SGFD) method with the SGLFD method by the dispersion curves for different orders, time intervals, and velocities.

Figure 1 shows the variation of ε with frequency for the different order. This figure demonstrates that dispersion decreases with the increase of the order for the SGFD and SGLFD methods. Note that

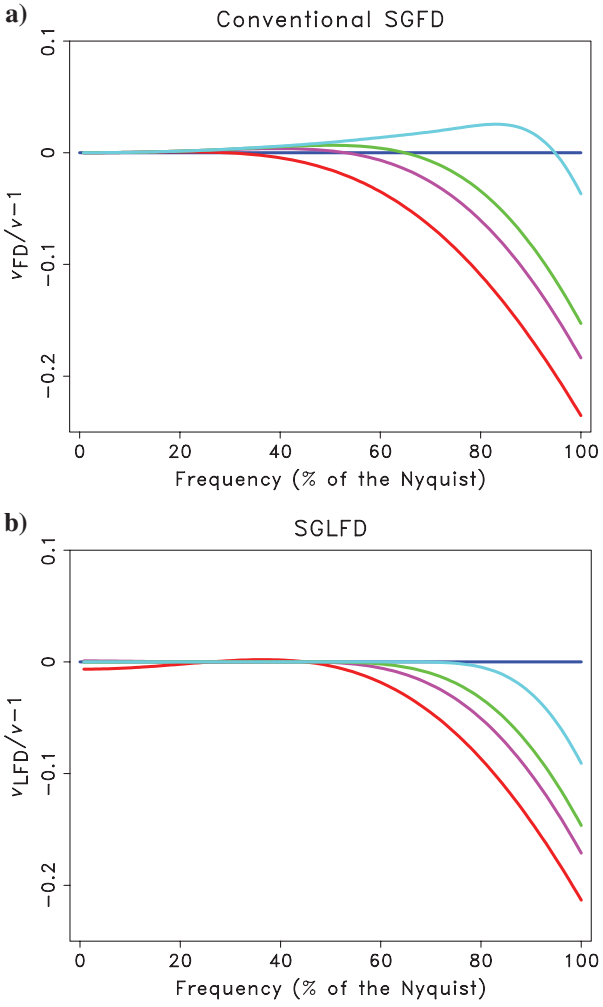

Figure 1. Plot of 1D dispersion curves of (a) the conventional SGFD method and (b) the SGLFD method for different orders, fourth-order (red, $2L = 4$), sixth-order (pink, $2L = 6$), eighth-order (green, $2L = 8$), 16th-order (blue, $2L = 16$), time interval $\Delta t = 1$ ms, space interval $\Delta_x = 10$ m, velocity $v = 3000$ m/s.

in the SGFD method, increases of order decrease the magnitude of the dispersion error without increasing the area where ε nearly equals 0. Compared with the SGFD method, the SGLFD method is highly accurate in a wider range of wavenumbers. Figure 2 shows the variation of ε with frequency for the difference time interval. From this figure, we can see that the dispersion becomes stronger when the SGFD method uses a larger time interval. Moreover, if a large time interval is used, such as $\Delta t = 2.5$ ms in this example, the SGFD method will be unstable. However, for the SGLFD method, its dispersion mainly depends on the frequency. Compared with the SGFD method, the SGLFD method keeps high accuracy for different time intervals (up to 70% of the Nyquist frequency). Figure 3 illustrates the effect of velocity on dispersion. Note that for the SGFD method, its dispersion curves change greatly with the variation of velocity. Compared with the SGFD method, the SGLFD method is more stable and accurate in a wider range of frequencies (up to 70% of the Nyquist frequency). In the previous examples, we used least-squares to fit to nearly 67% of the Nyquist frequency.

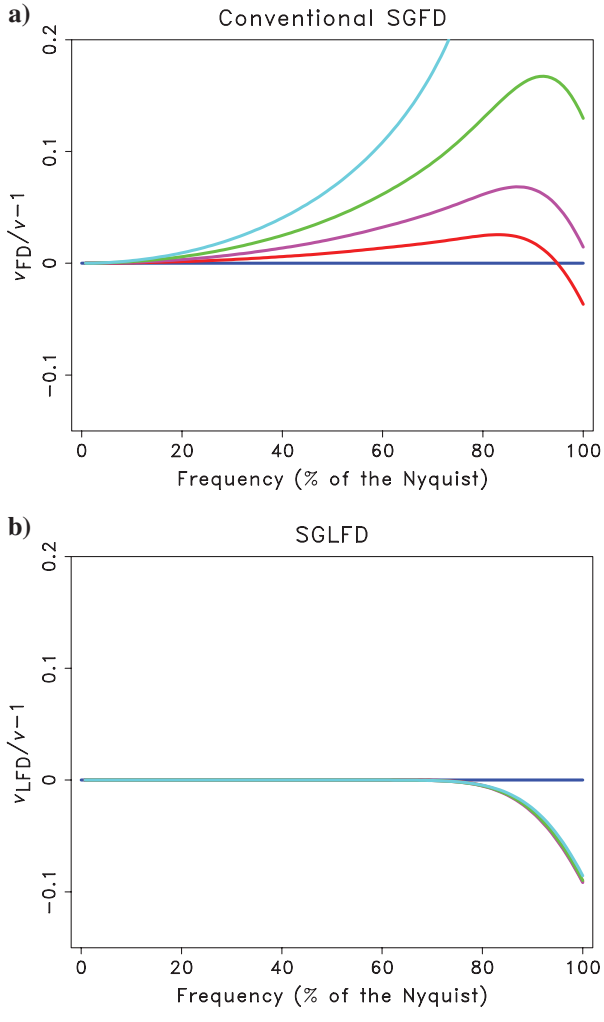

Figure 2. Plot of 1D dispersion curves of (a) the conventional SGFD method and (b) the SGLFD method for different time intervals: $\Delta t = 1$ ms (red), $\Delta t = 1.5$ ms (pink), $\Delta t = 2$ ms (green), $\Delta t = 2.5$ ms (blue), $\Delta x = 10$ m, $v = 3000$ m/s, $2L = 16$.

COMPARISON OF ACCURACY BETWEEN THE CONVENTIONAL SGFD METHOD AND THE LOWRANK METHODS

The study of accuracy is important especially for the heterogeneous media. However, for lowrank methods, it is hard to derive the theoretical accuracy order as what the Taylor-series expansion based SGFD method usually did. In this section, we compare the accuracy of the conventional SGFD method and the new lowrank methods numerically. We focus on the variable velocity case in the following analysis.

A simple illustration of the accuracy

We first use the simple 1D example shown in Figure 4 to demonstrate the accuracy of the SGL and SGLFD methods when they are used to calculate the partial derivatives in equation 9. The velocity increases linearly from 1000 to 2275 m/s. The rank is two for lowrank decomposition, assuming a 1 ms time step. The exact kx-space operator $\partial/\partial^+ x$ in equation 9 is shown in Figure 4a. Figure 4b–4d displays errors of approximation operators of SGL,

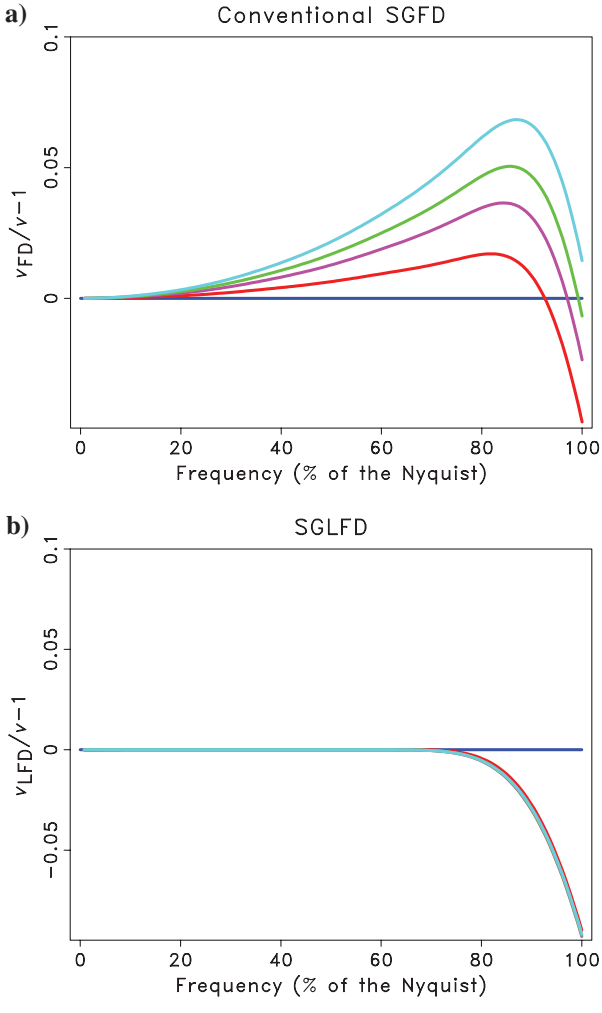

Figure 3. Plot of 1D dispersion curves of (a) the conventional SGFD method and (b) the SGLFD method for different velocities: $v = 2500$ m/s (red), $v = 3500$ m/s (pink), $v = 4000$ m/s (green), $\Delta t = 4500$ m/s (blue), $\Delta t = 1$ ms, $\Delta x = 10$ m, $2L = 16$.

SGLFD, and conventional SGFD, respectively. Figure 5 shows the middle column of the error matrix. The errors of SGL and SGLFD are significantly smaller than those of SGFD.

Error analysis using the method of manufactured solutions

Next we use the method of manufactured solutions (MMS) (Salari and Knupp, 2000) to analyze the numerical error of the proposed methods. The MMS provides an approach to designing exact reference solutions for wave equations in heterogeneous media. We couple the use of manufactured solutions with mesh refinement to plot the error curve for each method. To begin our investigation, we consider the system of 1D first-order wave equations:

$$\frac{\partial u(x,t)}{\partial t} = -\frac{1}{\rho(x)}\frac{\partial p(x,t)}{\partial x} + s_u(x,t),$$
$$\frac{\partial p(x,t)}{\partial t} = -\rho(x)v^2(x)\frac{\partial u(x,t)}{\partial x} + s_p(x,t), \qquad (21)$$

which are subjected to appropriate boundary and initial conditions, where s_u and s_p represent the inject source terms for the particle velocity u and pressure p, respectively. For this study, we are interested in the governing equation. We choose a Gaussian pulse as the solution of the pressure and particle velocity in variable velocity media (Ober et al., 2009),

$$u(x,t) = p(x,t) = e^{-\lambda^2(x-x_0-v(x)t)^2}, \qquad (22)$$

where λ is the wavelength of the Gaussian pulse, x_0 is the source location, and $v(x)$ is the variable velocity. It is easy to derive the corresponding source terms from equations 21 and 22:

$$s_u(x,t) = 2\lambda^2[x-x_0-v(x)t]\left[v(x) + \frac{v'(x)t-1}{\rho(x)}\right]p(x,t),$$
$$s_p(x,t) = 2\lambda^2[x-x_0-v(x)t][v(x) + \rho(x)v^2(x)(v'(x)t-1)]p(x,t). \qquad (23)$$

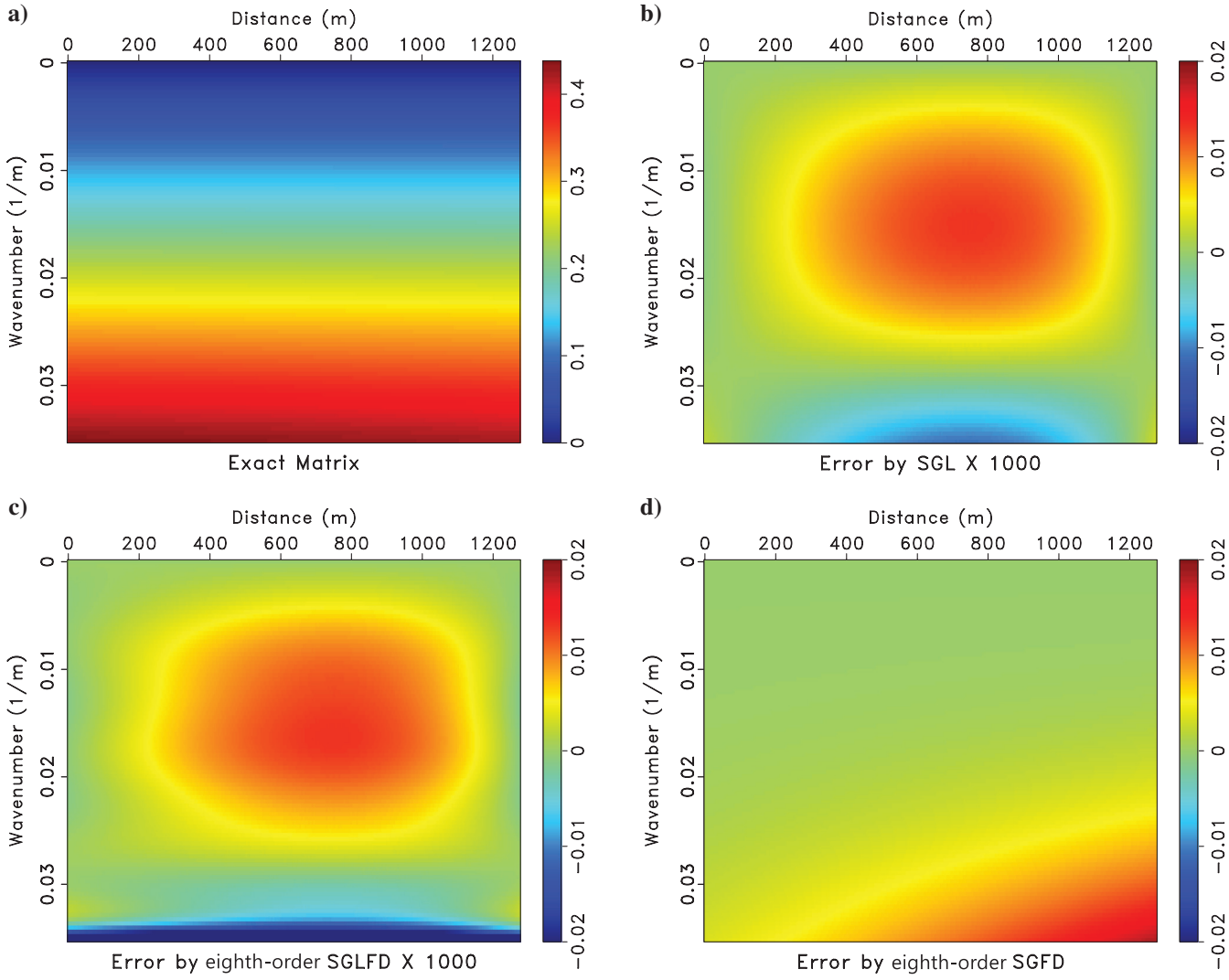

Figure 4. (a) The kx-space operator $\partial/\partial^+ x$ for 1D linearly increasing velocity model. (b) Error of the SGL operator. (c) Error of the eighth-order SGLFD operator. (d) Error of the eighth-order SGFD operator.

For the numerical solution, accuracy is often affected by various factors. In this study, we examine the numerical error of the proposed methods when using different temporal and spatial discretization and wavelets of different dominant frequencies.

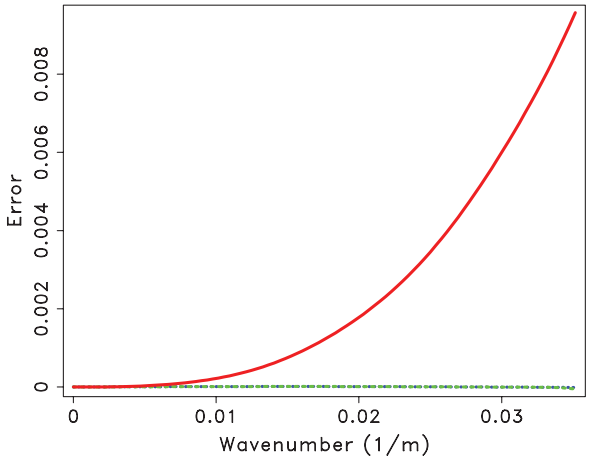

Figure 5. Middle column of the error matrix. (Blue dashed line, SGL operator; green dotted line, the eighth-order SGLFD operator; and red solid line, the eighth-order SGFD operator.)

The velocity we used here increases with x, defined as $v(x) = 2.1 + 0.1x^2(\mathrm{km/s})$. Its gradient is $v'(x) = 0.2x$, correspondingly. We use constant density in this experiment. Figure 6a shows the root-mean-square (rms) errors of the wavefields for a different time interval. For all these calculations, we keep the space interval $\Delta x = 25$ m as constant. The blue dashed line and green dotted line indicate the errors of the SGL and SGLFD methods, respectively, and the red solid line plots the errors of the traditional SGFD method. Compared with the traditional SGFD method, the proposed lowrank methods correct the distortion caused by increasing Δt. They exhibit a high accuracy in time. Figure 6b shows the recorded trace at the x of 4 km for $\Delta t = 4$ ms. The black solid line corresponds to the exact solution generated by MMS. The colors of the remaining lines have the same meanings as in Figure 6a. Numerical dispersion is more visible when Δt is increased; this effect is much less significant in our methods.

Figure 7a shows the rms errors of the wavefields for different space intervals. We use a small time interval $\Delta t = 0.4$ ms to keep the time error small. Figure 7b shows the recorded data for $\Delta x = 40$ m. The first-order kx-space operators (equation 9) have a high accuracy in space, which makes the error of SGL method increase slowly when Δx increase. The coefficients of the SGLFD are obtained by applying least-squares fitting to the SGL method. The error from the least-squares fitting makes the SGLFD method less accurate than the SGL method. On the other hand,

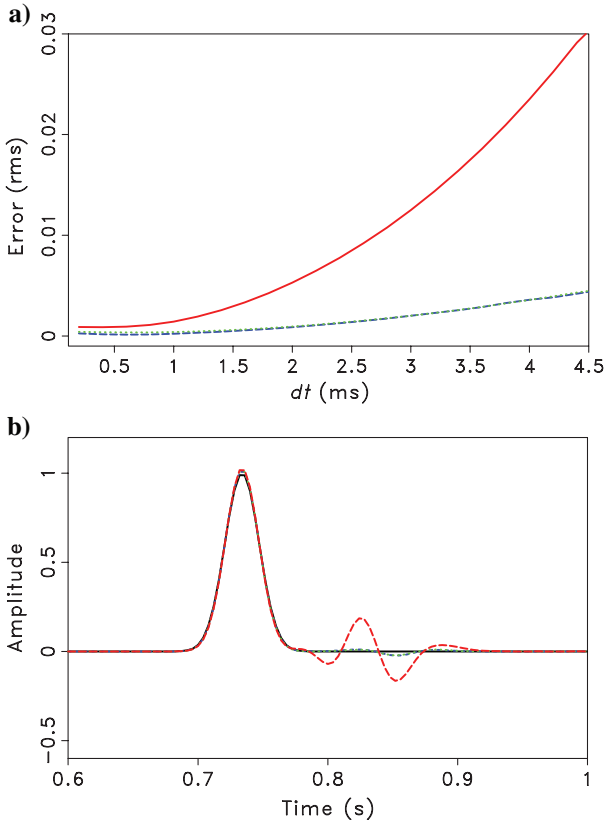

Figure 6. (a) The rms errors as a function of the time interval. (b) Recorded data for $\Delta t = 4$ ms. (Blue dashed line, SGL method; green dotted line, SGLFD method; red solid line, SGFD method; and black solid line, MMS.)

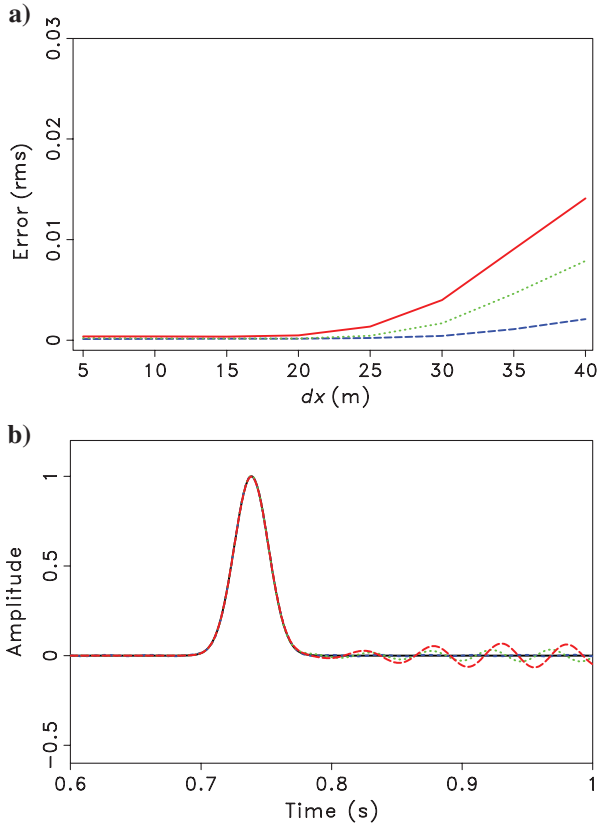

Figure 7. (a) The rms errors as a function of the space interval. (b) Recorded data for $\Delta x = 40$ m. (Blue dashed line, SGL method; green dotted line, SGLFD method; red solid line, SGFD method; and black solid line, MMS.)

the coefficients of lowrank FD are optimized and autoadapted to variations in velocity, which makes it significantly more accurate than the SGFD method.

In applications of seismic-wave extrapolation, temporal and spatial intervals are often increased at a certain ratio for saving computational cost. Figure 8 shows the error curves for a temporal and spatial refinement study where Δx and Δt are increased simultaneously. We define the Courant-Friedrichs-Lewy (CFL) number as $\alpha = v_{\max}\Delta t/\Delta x$ to specify the stability condition, where $v_{\max}$ is

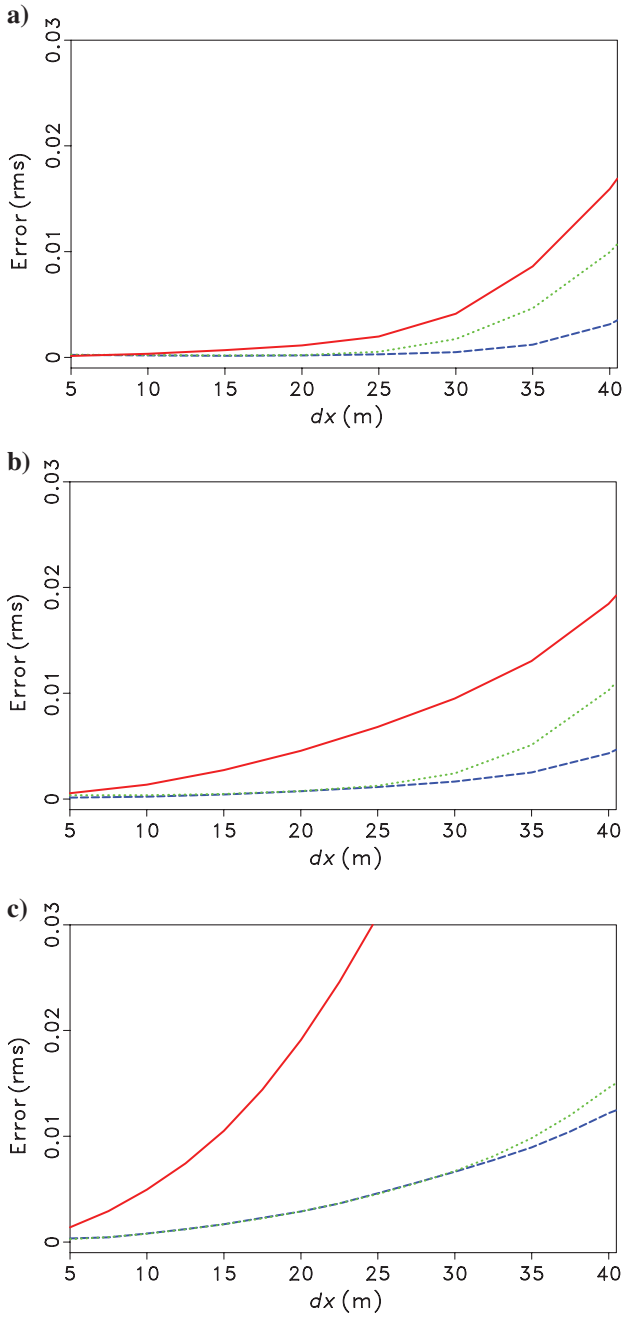

Figure 8. The rms errors for CFL number (a) $\alpha = 0.2$, (b) $\alpha = 0.4$, and (c) $\alpha = 0.8$. (Blue dashed line, SGL method; green dotted line, SGLFD method; and red solid line, SGFD method.)

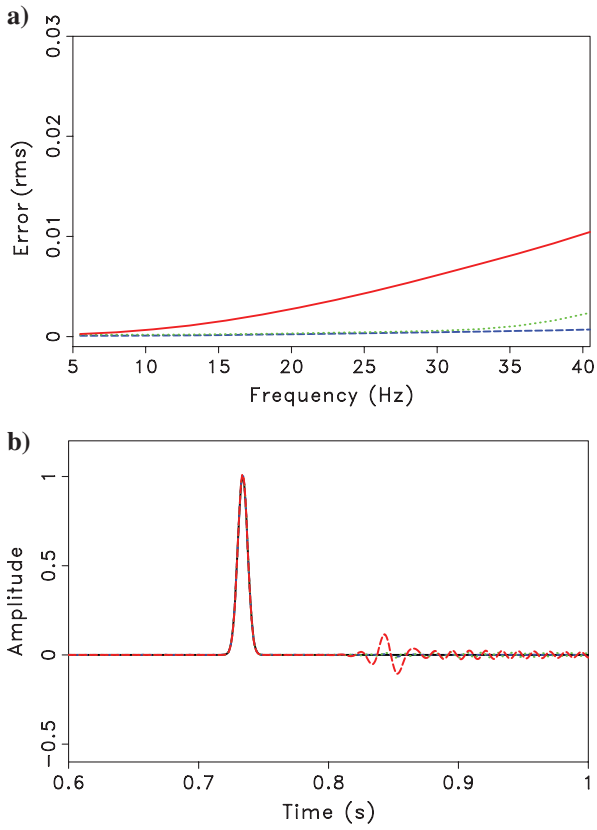

Figure 9. (a) The rms errors as a function of the dominant frequency of the source wavelet. (b) Recorded data for frequency of 40 Hz. (Blue dashed line, SGL method; green dotted line, SGLFD method; red solid line, SGFD method; and black solid line, MMS.)

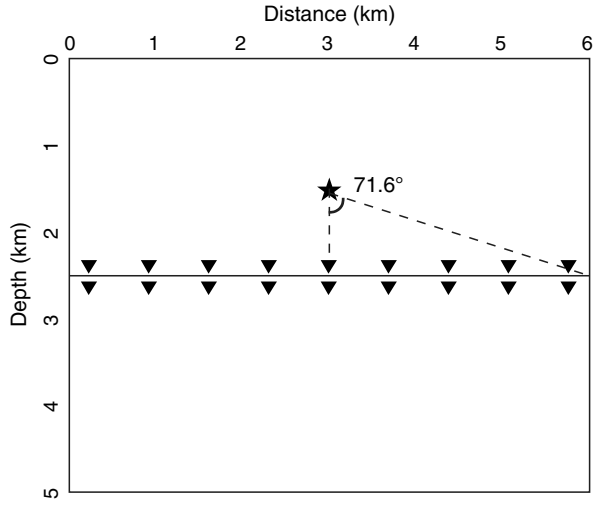

Figure 10. The geometry of the planar interface model. The star denotes the source location, and the triangles denote the receiver locations. The values of the incident angle along the planar interface are between 0° and 71.6°.

the maximum velocity. Figure 8a shows the rms errors for $\alpha = 0.2$. Figure 8b shows the rms error of $\alpha = 0.4$, whereas Figure 8c for $\alpha = 0.8$. The colors of the lines have the same meanings as indicated before. We can see that the errors increase with the CFL number α. This increase is especially significant for SGFD method. The SGL and SGLFD methods keep high accuracy for a larger scale of temporal and spatial intervals than does SGFD.

Seismic exploration techniques, such as prestack depth migration or full-waveform inversion, need the modeling engine, which remains highly accurate for a wideband seismic wavelet. The numerical dispersion can be serious for a high-frequency source. Figure 9a compares the accuracy of different methods for different source frequencies. The meanings of different line colors are the same as before. Figure 9b shows the recorded data with a source frequency of 40 Hz. It can be seen that the SGFD method has a visible dispersion, whereas SGL and SGLFD methods remain almost dispersion free.

The accuracy estimation for planar interface

For seismic modeling, it is important to estimate the accuracy of the proposed methods for heterogeneous media, especially for the amplitude variation with offset or amplitude variation with angle effects of reflected or transmitted wavefields along the interface. The theoretical analysis of this feature can be complicated. Here, we provide a simple numerical test to illustrate the accuracy of the proposed methods. We design a planar interface model, which is defined on a grid system of 601×501 with a space interval of 10 m in the horizontal and vertical directions, as shown in Figure 10. The planar interface is aligned with the vertical 251st grid. The velocities of the upper and lower layers are designed as 4000 and 2000 m/s to avoid critical reflection. We use a constant density $\rho = 1700$ kg/m^3. We synthesize a shot record to examine the accuracy of our methods. The source is located at the position of 3000 m in the horizontal direction and 1500 m in the vertical direction. Thus, the maximum incident angle is 71.6°. We place two receiver lines above and below the interface and measure the amplitudes of incident, reflected, and transmitted wavefields. The reflection coefficient is given by the ratio of amplitudes of the reflected wavefield and the incident wavefield. The transmission coefficient is given by the ratio of amplitudes of the

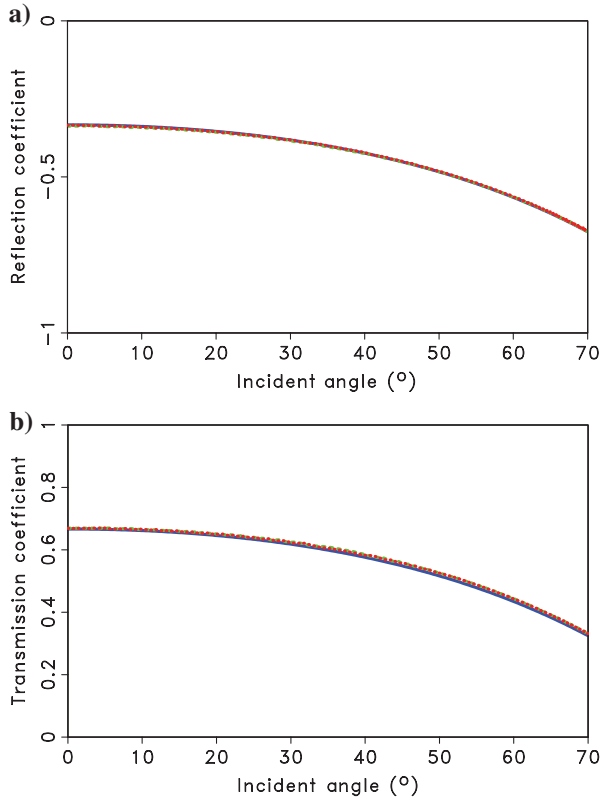

Figure 11. Comparison of reflection (a) and transmission (b) coefficients calculated by the SGL method (red dashed line) and the SGLFD method (green dashed line) with the theoretical values (blue solid line).

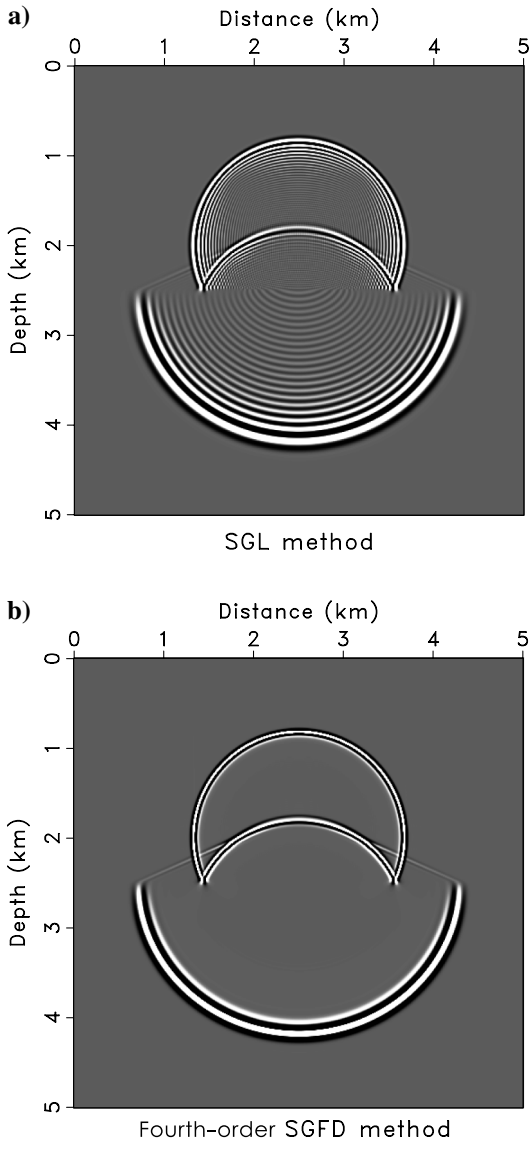

Figure 12. Wavefield snapshot in a two-layer model with variable density and velocity using the (a) SGL and (b) SGFD methods.

transmitted and reflected wavefields. Figure 11 compares the reflection and transmission coefficients calculated by the SGL and SGLFD methods with the theoretical values calculated by solving the Zoeppritz equations. From this figure, we see that the reflection and transmission coefficients calculated by the SGL and SGLFD method match well with the theoretical values. Thus, the SGL and SGLFD methods appear sufficiently accurate to provide correct dynamic information of wavefields.

NUMERICAL EXAMPLES

2D examples of a two-layer model

To test the performance of the proposed methods with a rough velocity model, we use a two-layer model with high velocity and density contrasts. The model is defined on a 501×501 grid, with $\Delta x = \Delta z = 10$ m and $\Delta t = 1.5$ ms. The velocities of the upper and lower layers are 1.3 and 3.2 km/s. The densities of the upper and lower layers are 1.7 and 2.7 g/cm^3, respectively. A point source with a Ricker wavelet with dominant frequency of 20 Hz is located in the center of the model at a depth of 0.2 km. The maximum frequency ($f_{\max}$) is around 60 Hz. Following Song et al. (2013), we still use the CFL number α to specify the stability and define dispersion factor as $\beta = v_{\min}/(f_{\max}\Delta x)$ to indicate the sample points per wavelength, where $v_{\min}$ is the minimum velocity of the model. For modeling with the above parameters, $\alpha = 0.32$ and $\beta = 2.2$. Figure 12 shows a wavefield snapshot in a two-layer model with a time interval of 1 ms. Figure 13 displaces two vertical traces at a distance of 2.5 km selected from the wavefield snapshots shown in Figure 12. The top trace is calculated using a fourth-order SGFD method. The bottom trace is calculated using SGL method proposed in this paper. Note the obvious numerical dispersion of the SGFD method. Figure 14 shows a wavefield snapshot generated by SGLFD with a time interval equal to 2 ms. At this time interval, the SGFD method becomes unstable.

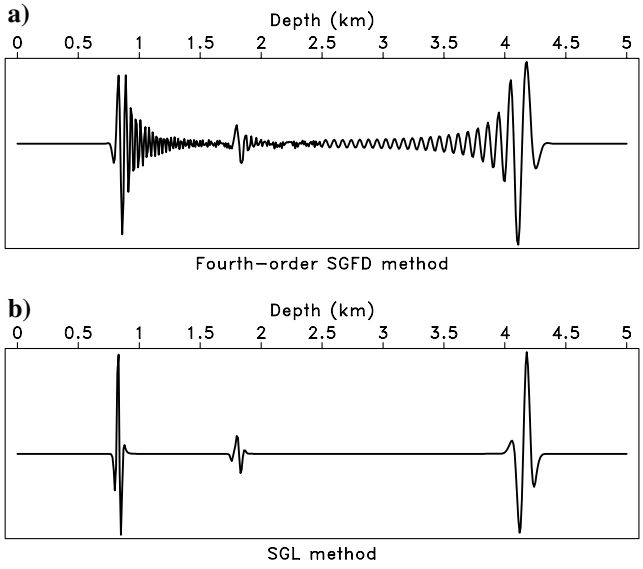

Figure 13. Vertical trace at a distance of 2.5 km selected from the snapshots shown in Figure 12 for comparison of the (a) SGFD and (b) SGL methods.

Example of the BP model

Finally, we test the proposed methods in a complex velocity model. Figure 15 shows a part of the BP-2004 model, which is a complicated model containing a salt body and sharp velocity and density contrasts on the flanks of the salt body (Billette and Brandsberg-Dahl, 2004). We use a Ricker wavelet at a point source with a dominant frequency of 20 Hz ($f_{\max} \approx 60$ Hz). The horizontal grid size Δx and vertical grid size Δz are 12.5 m, and the time step is 1.5 ms; thus, $\alpha \approx 0.57$ and $\beta \approx 1.98$. Figure 16 shows the wavefield snapshot in the BP model generated by SGL method and sixth-order SGLFD with a rank of three. This experiment confirms that the staggered-grid lowrank methods are able to handle sharp velocity and density variations.

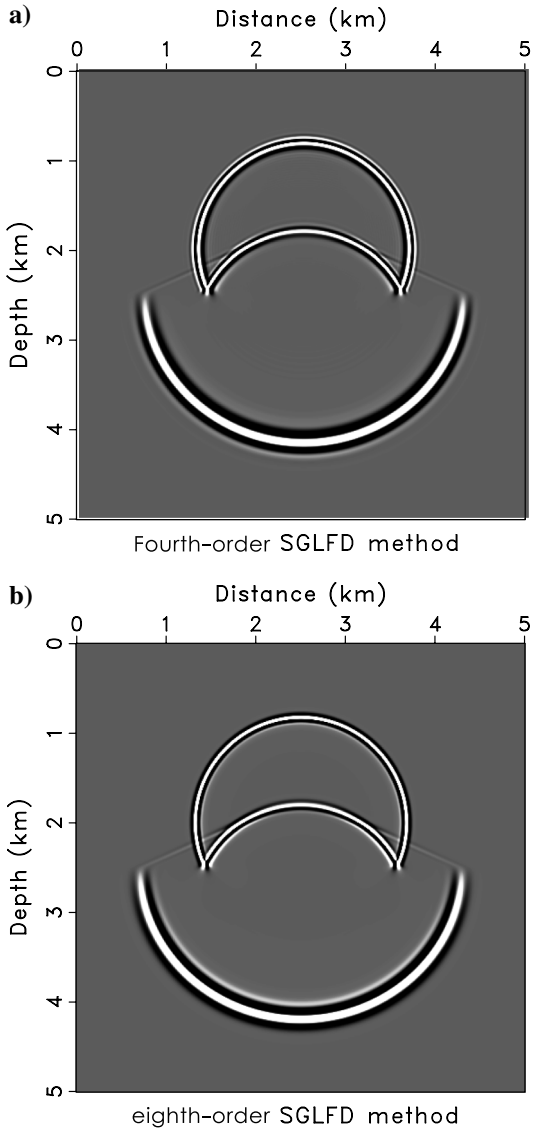

Figure 14. Wavefield snapshot in a two-layer model with variable density and velocity using (a) fourth-order SGLFD method and (b) eighth-order SGLFD method.

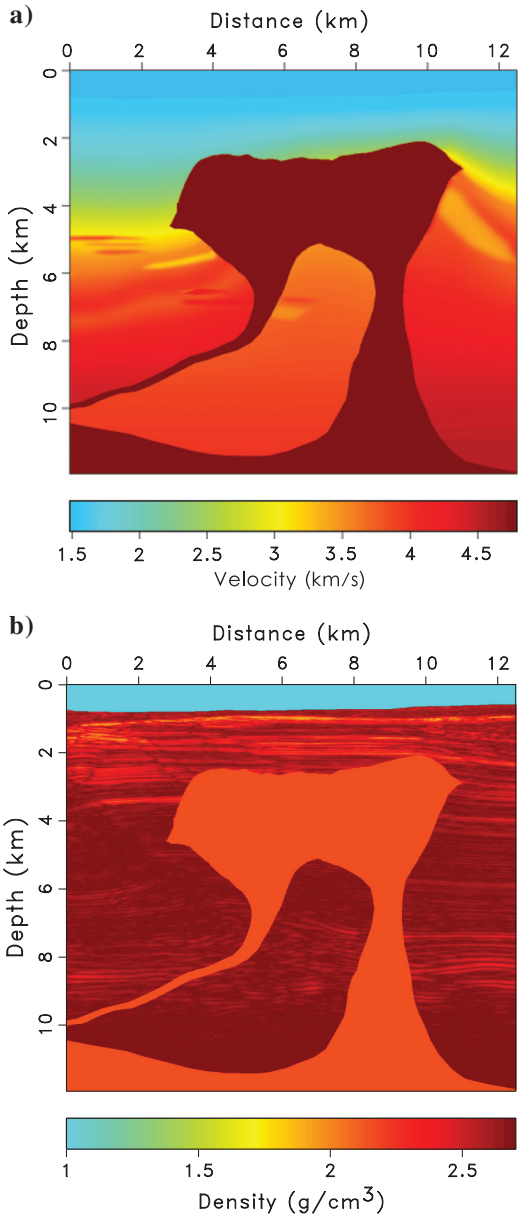

Figure 15. BP model: (a) velocity and (b) density.

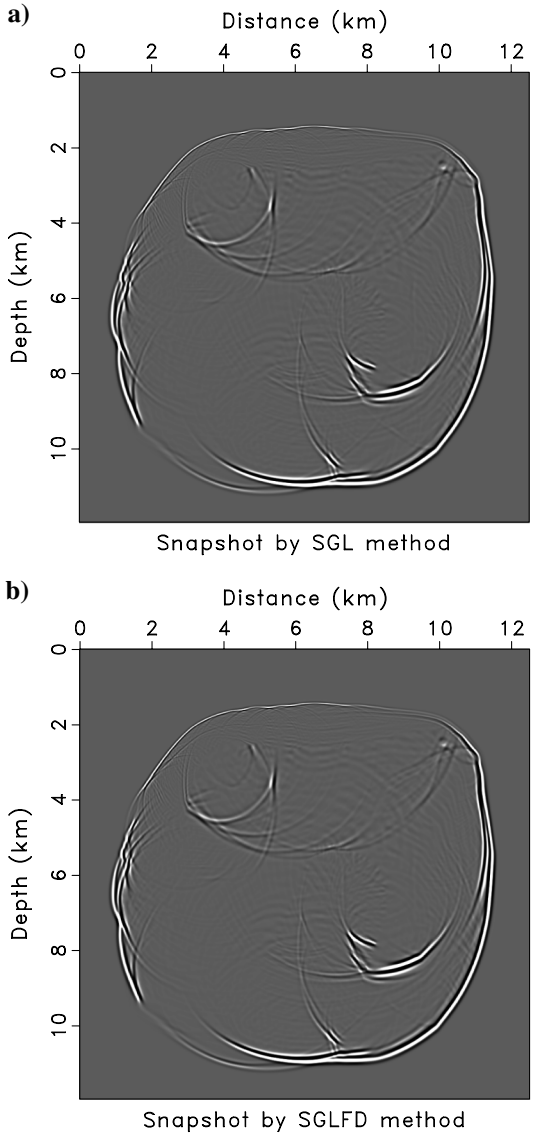

Figure 16. Wavefield snapshot modeled through for the BP model using the (a) SGL and (b) SGLFD methods.

CONCLUSIONS

FD and spectral methods are the two most popular wavefield-extrapolation approaches for seismic modeling and seismic-wavefield imaging. To handle variable density and velocity in seismic modeling or RTM, we proposed an SGL method by applying lowrank decomposition to first-order kx-space propagation operators on a staggered grid. The cost of the new method amounts to using a small number of FFTs, which corresponds to the approximation rank. On the basis of the SGL method, we also designed the SGLFD method, which extends the lowrank FDs from a case of constant density to one of variable density. This approach promises higher accuracy and better stability than those of the traditional, explicit staggered-grid FD methods. We tested the proposed methods using the MMS and concluded that they retained high accuracy for large temporal and spatial intervals or high-frequency sources. Results for the synthetic models illustrate that our proposed methods are highly accurate for heterogeneous media and can handle sharp velocity and density variations. Although the proposed methods are focused on the acoustic case, they can also be extended in principle to elastic, anisotropic, or attenuating media. The methods can be used for seismic modeling or RTM.

ACKNOWLEDGMENTS

We appreciate the support of the China State Scholarship Fund, the Natural Science Foundation of China (41074087, 41174100), and the Fundamental Research Funds for the Central Universities (11CX06002A). We thank KAUST and the Texas Consortium for Computational Seismology for partial financial support. We also thank all developers of the Madagascar open-source software

package (http://ahay.org). We thank the Texas Advanced Computing Center for providing the supercomputing resources used in this study.

REFERENCES

Billette, F. J., and S. Brandsberg-Dahl, 2004, The 2004 BP velocity benchmark: 67th Annual International Conference and Exhibition, EAGE, Extended Abstracts, B305.

Bohlen, T., 2002, Parallel 3-D viscoelastic finite difference seismic modelling: Computers & Geosciences, **28**, 887–899, doi: 10.1016/S0098-3004(02)00006-7.

Chu, C., and P. L. Stoffa, 2011, Application of normalized pseudo-Laplacian to elastic wave modeling on staggered grids: Geophysics, **76**, no. 5, T113–T121, doi: 10.1190/geo2011-0069.1.

Chu, C., P. L. Stoffa, and R. Seif, 2009, 3D elastic wave modeling using modified high-order time stepping schemes with improved stability condition: 79th Annual International Meeting, SEG, Expanded Abstracts, 2662–2666.

Dablain, M. A., 1986, The application of high-order differencing to the scalar wave equation: Geophysics, **51**, 54–66, doi: 10.1190/1.1442040.

Du, X., P. Fowler, and R. Fletcher, 2014, Recursive integral time-extrapolation methods for waves: A comparative review: Geophysics, **79**, no. 1, T9–T26, doi: 10.1190/geo2013-0115.1.

Engquist, B., and L. Ying, 2009, A fast directional algorithm for high frequency acoustic scattering in two dimensions: Communications in Mathematical Sciences, **7**, 327–345, doi: 10.4310/CMS.2009.v7.n2.a3.

Etgen, J., 1986, High order finite-difference reverse time migration with the two way non-reflecting wave equation: Stanford Exploration Project, **48**, 133–146.

Etgen, J., and S. Brandsberg-Dahl, 2009, The pseudo-analytical method: Application of pseudo-Laplacians to acoustic and acoustic anisotropic wave propagation: 79th Annual International Meeting, SEG, Expanded Abstracts, 2552–2556.

Finkelstein, B., and R. Kastner, 2007, Finite difference time domain dispersion reduction schemes: Journal of Computational Physics, **221**, 422–438, doi: 10.1016/j.jcp.2006.06.016.

Fomel, S., P. Sava, I. Vlad, Y. Liu, and V. Bashkardin, 2013a, Madagascar: Open-source software project for multidimensional data analysis and reproducible computational experiments: Journal of Open Research Software, **1**, e8, doi: 10.5334/jors.ag.

Fomel, S., L. Ying, and X. Song, 2010, Seismic wave extrapolation using a lowrank symbol approximation: 80th Annual International Meeting, SEG, , Expanded Abstracts, 3092–3096.

Fomel, S., L. Ying, and X. Song, 2013b, Seismic wave extrapolation using lowrank symbol approximation: Geophysical Prospecting, **61**, 526–536, doi: 10.1111/j.1365-2478.2012.01064.x.

Fowler, P., X. Du, and R. Fletcher, 2010, Recursive integral time extrapolation methods for scalar waves: 80th Annual International Meeting, SEG, Expanded Abstracts, 3210–3215.

Kindelan, M., A. Kamel, and P. Sguazzero, 1990, On the construction and efficiency of staggered numerical differentiators for the wave equation: Geophysics, **55**, 107–110, doi: 10.1190/1.1442763.

Levander, A. R., 1988, Fourth-order finite-difference P-SV seismograms: Geophysics, **53**, 1425–1436, doi: 10.1190/1.1442422.

Liu, Y., 2013, Globally optimal finite-difference schemes based on least squares: Geophysics, **78**, no. 4, T113–T132, doi: 10.1190/geo2012-0480.1.

Liu, Y., and M. K. Sen, 2009, An implicit staggered-grid finite-difference method for seismic modelling: Geophysical Journal International, **179**, 459–474, doi: 10.1111/j.1365-246X.2009.04305.x.

Madariaga, R., 1976, Dynamics of an expanding circular fault: Bulletin of the Seismological Society of America, **66**, 639–666.

Mast, T. D., L. P. Souriau, D. Liu, M. Tabei, A. I. Nachman, and R. C. Waag, 2001, A *k*-space method for large-scale models of wave propagation in tissue: IEEE Transactions on Ultrasonics, Ferroelectrics and Frequency Control, **48**, 341–354, doi: 10.1109/58.911717.

Moczo, P., J. Kristek, and V. Vavrycuk, 2002, 3D heterogeneous staggered-grid finite-difference modeling of seismic motion with volume harmonic and arithmetic averaging of elastic moduli and densities: Bulletin of the Seismological Society of America, **92**, 3042–3066, doi: 10.1785/0120010167.

Ober, C. C., S. S. Collis, B. B. Waanders, and C. Marcinkovich, 2009, Method of manufactured solutions for the acoustic wave equation: 79th Annual International Meeting, SEG, Expanded Abstracts, 3615–3619.

Operto, S., J. Virieux, P. Amestoy, J. Y. Amestoy, J. Y. Giraud, and H. B. H. Ali, 2007, 3D finite-difference frequency-domain modeling of visco-acoustic wave propagation using a massively parallel direct solver: A feasibility study: Geophysics, **72**, no. 5, SM195–SM211, doi: 10.1190/1.2759835.

Reshef, M., D. Kosloff, M. Edwards, and C. Hsiung, 1988, Three-dimensional acoustic modeling by the Fourier method: Geophysics, **53**, 1175–1183, doi: 10.1190/1.1442557.

Robertsson, J. O. A., J. O. Blanch, and W. W. Symes, 1994, Viscoelastic finite-difference modeling: Geophysics, **59**, 1444–1456, doi: 10.1190/1.1443701.

Salari, K., and P. Knupp, 2000, Code verification by the method of manufactured solutions: Sandia National Laboratories, report SAND2000-1444.

Song, X., and S. Fomel, 2011, Fourier finite-difference wave propagation: Geophysics, **76**, no. 5, T123–T129, doi: 10.1190/geo2010-0287.1.

Song, X., S. Fomel, and L. Ying, 2013, Lowrank finite-differences and lowrank Fourier finite-differences for seismic wave extrapolation: Geophysical Journal International, **193**, 960–969, doi: 10.1093/gji/ggt017.

Song, X., K. Nihei, and J. Stefani, 2012, Seismic modeling in acoustic variable-density media by Fourier finite differences: 82nd Annual International Meeting, SEG, Expanded Abstracts, doi: 10.1190/segam2012-0723.1.

Soubaras, R., and Y. Zhang, 2008, Two-step explicit marching method for reverse time migration: 78th Annual International Meeting, SEG, Expanded Abstracts,2272–2276.

Tabei, M., T. D. Mast, and R. C. Waag, 2002, A *k*-space method for coupled first-order acoustic propagation equations: Journal of the Acoustical Society of America, **111**, 53–63, doi: 10.1121/1.1421344.

Takeuchi, N., and R. J. Geller, 2000, Optimally accurate second order time-domain finite difference scheme for computing synthetic seismograms in 2-D and 3-D media: Physics of the Earth and Planetary Interiors, **119**, 99–131, 10.1016/S0031-9201(99)00155-7.

Tal-Ezer, H., D. Kosloff, and Z. Koren, 1987, An accurate scheme for seismic forward modeling: Geophysical Prospecting, **35**, 479–490, doi: 10.1111/j.1365-2478.1987.tb00830.x.

Virieux, J., 1984, SH-wave propagation in heterogeneous media: Velocity-stress finite-difference method: Geophysics, **49**, 1933–1942, doi: 10.1190/1.1441605.

Virieux, J., 1986, P-SV wave propagation in heterogeneous media: Velocity-stress finite-difference method: Geophysics, **51**, 889–901, doi: 10.1190/1.1442147.

Wards, B., G. Margrave, and M. Lamoureux, 2008, Phase-shift time-stepping for reverse-time migration: 78th Annual International Meeting, SEG, Expanded Abstracts, 2262–2266.

Wu, W., L. R. Lines, and H. Lu, 1996, Analysis of high-order, finite-difference schemes in 3-D reverse-time migration: Geophysics, **61**, 845–856, doi: 10.1190/1.1444009.

Zhang, Y., and G. Zhang, 2009, One-step extrapolation method for reverse time migration: Geophysics, **74**, no. 4, A29–A33, doi: 10.1190/1.3123476.

Zhang, Y., G. Zhang, D. Yingst, and J. Sun, 2007, Explicit marching method for reverse time migration: 76th Annual International Meeting, SEG, Expanded Abstracts, 2300–2304.